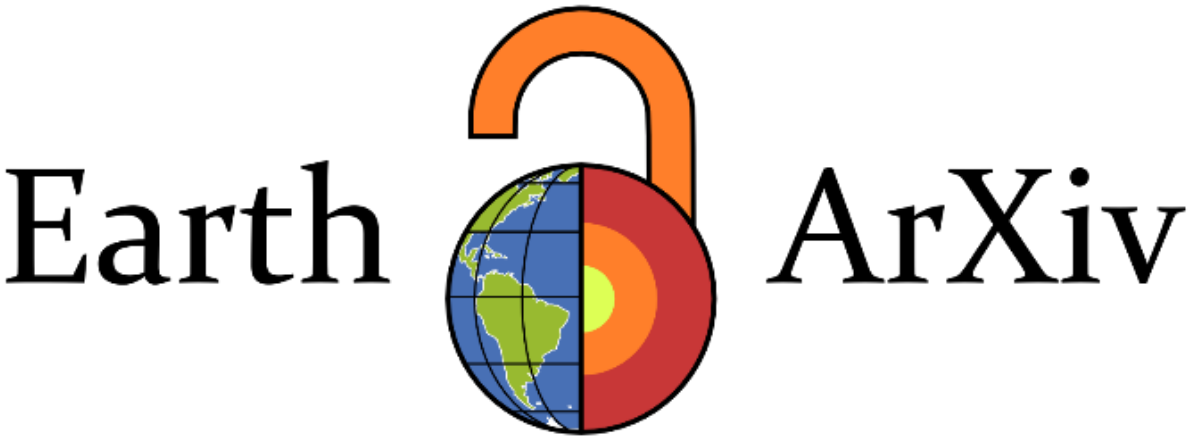

Beyond a Single Risk Score: Posterior Rank Uncertainty in Wildfire Exposure of Transmission Corridors

Wenxing Yi

July 2026

Abstract

Transmission-line wildfire decisions often require segment-level triage, while equipment-condition, outage, and inspection records are not public. This paper presents a reproducible public-data framework for retrospective external wildfire exposure ranking of California transmission-line segments. The line segments are treated only as receptor assets, not as ignition sources, failure points, outage causes, or responsibility units. Using California Energy Commission transmission lines, CAL FIRE FRAP fire perimeters and cause fields, gridMET weather summaries, LANDFIRE LF2024 fuel and canopy layers, and USGS 3DEP terrain, the workflow constructs a 2017–2023 segment-year panel for the Northern Sierra and Southern Cascades. The main label excludes CAL FIRE CAUSE = 11, Electrical Power, to reduce conflation between external wildfire exposure and electrical-power fire cause. A Bayesian logistic exposure model is compared with a deterministic public physics score and machine-learning baselines under a 2022–2023 temporal holdout. Bayesian Laplace and L2 logistic discrimination are close; the Bayesian contribution is therefore framed as posterior exceedance probability and posterior top-decile rank probability for rare-event triage, not as universal classification superiority. Probability scores only modestly improve on a training-prevalence constant baseline, so posterior rank probability is emphasized as the primary decision output.

1 Introduction

Wildfire activity in the western United States is strongly linked to fuel aridity and changing fire-weather conditions (Abatzoglou and Williams, 2016). Wildfires also create direct and indirect risks for electricity infrastructure and grid operations (Dale et al., 2018; Panossian and Elgindy, 2023). For transmission corridors, screening decisions are often made at the segment scale with incomplete public information about asset condition, protection systems, inspection history, vegetation work, and outage outcomes.

Existing work addresses both grid-to-fire ignition risk and fire-to-grid infrastructure impacts. Electricity-infrastructure ignition models can rely on ignition, wire-down, and detailed asset data (Yao et al., 2022), whereas wildfire exposure and grid-impact studies address the consequences of fires for electricity systems (Dale et al., 2018; Panossian and Elgindy, 2023). This study is in the second category: it ranks external fire exposure for transmission-line receptor assets.

The public-data constraint is central. Private utility records can materially change both the prediction target and the feature set (Yao et al., 2022). This paper therefore does not estimate powerline-caused ignition probability, equipment failure, outage probability, damage, or legal responsibility. Electrical-power fire overlap is retained only as a diagnostic, because a perimeter-level cause field does not identify the exact ignition device or segment.

The methodological question is how to support rare-event triage when the output of interest is a ranked list. Deterministic public physics scores and machine-learning classifiers return useful point scores, but operational screening often asks whether a segment plausibly belongs in the high-exposure tail. A Bayesian decision layer answers this with posterior exceedance probability and posterior top-decile rank probability.

2 Study Area and Public Data

2.1 Study Area

The case study focuses on the Northern Sierra and Southern Cascades in California. Decision units are approximately 1 km transmission-line segments. The analysis panel spans 2017–2023 and uses segment-year rows so annual fire labels and annual observed environmental summaries are aligned. A fixed 1 km segment buffer is used for perimeter-overlap labels. Figure 1 shows the study region and receptor-asset segments.

2.2 Segment Construction

The study domain is the WGS84 bounding box $(-123.2, 38.6, -119.0, 41.8)$, covering the Northern Sierra and Southern Cascades. Vector processing is conducted in EPSG:3310. CEC transmission-line geometries are read within the study box, projected to EPSG:3310, filtered to remove missing and empty geometries, clipped to the study domain, and split at 1,000 m chainage intervals. Multipart LineStrings are iterated part by part, and terminal residual pieces are retained if they have positive length. The resulting segment layer is written in WGS84 for mapping, while 1 km buffers are constructed in EPSG:3310 for fire-perimeter overlap labels.

2.3 Public Data Sources

Table 1 summarizes the public data sources. The processed panel contains 11,255 line segments and 78,785 segment-year observations. CEC transmission lines provide receptor-asset geometries (California Energy Commission, 2026). CAL FIRE FRAP fire perimeters provide annual overlap labels (California Department of Forestry and Fire Protection, Fire and Resource Assessment Program, 2026). gridMET provides daily meteorological fields that are summarized annually (Abatzoglou, 2013). LANDFIRE provides static fuel and canopy context (Rollins, 2009); this workflow uses LF2024 (LANDFIRE, 2025), with product coding and decoded units following LANDFIRE documentation (LANDFIRE, 2026). Terrain covariates are derived from USGS 3DEP elevation data (U.S. Geological Survey, 2026).

3 Label Construction

Let i index line segments, t years, and j individual fire perimeters. Let B_i be the segment buffer and P_j be fire perimeter j. The main external exposure label is

$$y_{it}^{exo} = \mathbf{1}\left\{\exists j : \ \text{year}(j) = t, \ B_i \cap P_j \neq \emptyset, \ \text{CAUSE}_j \neq 11\right\}. \tag{1}$$

CAL FIRE CAUSE = 11 denotes Electrical Power. The exclusion in Equation 1 is used to avoid mixing external exposure with electrical-power fire cause in the main validation target. It does not assert that remaining fires cannot affect or be affected by transmission assets.

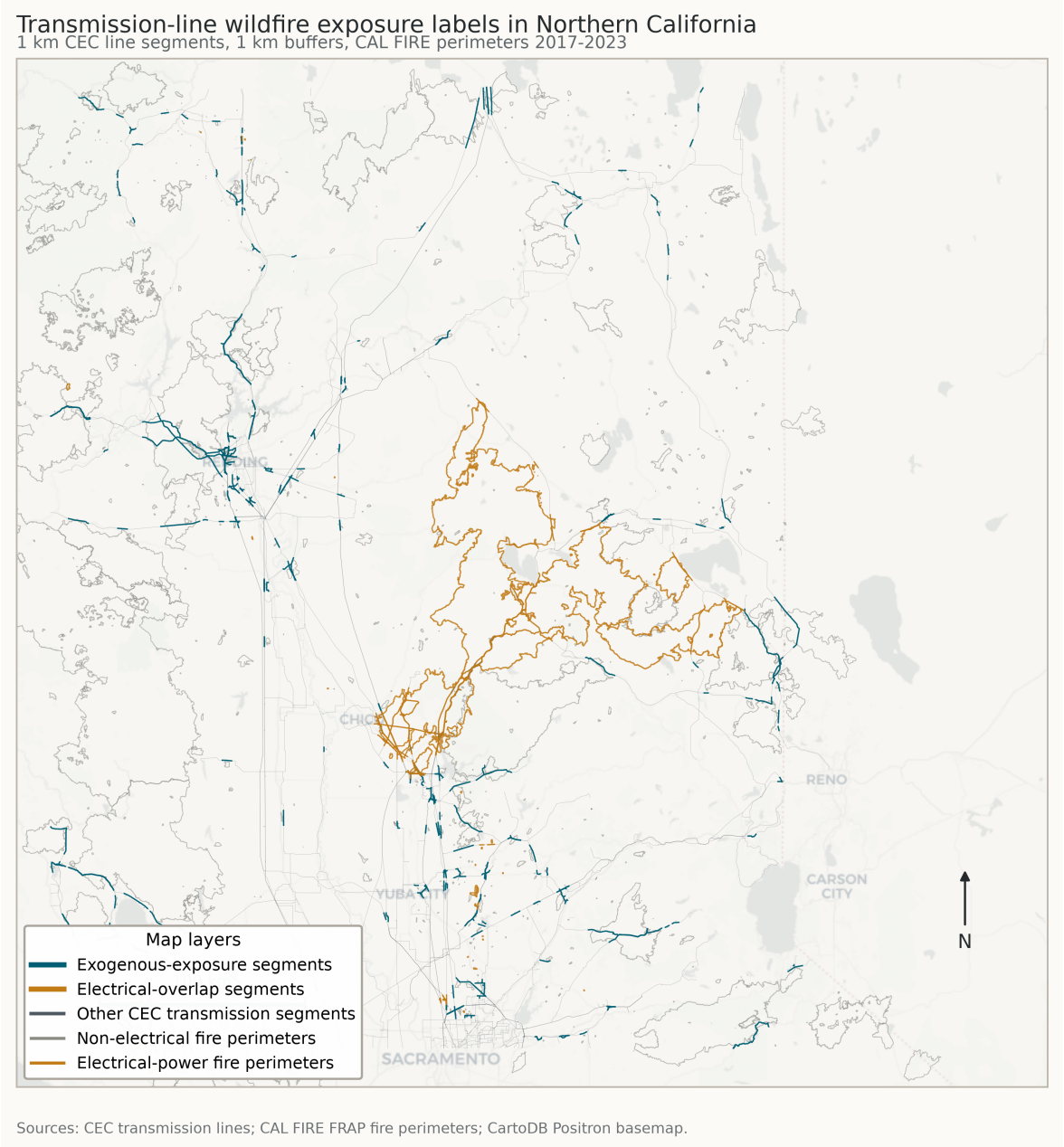

Figure 1: Study region, public transmission-line segments, and annual exposure labels.

Table 1: Public data sources and analytical roles.

Dataset	Source	Resolution / unit	Version or years	Role and caveat
Transmission lines	California Energy Commission	Public line geometry	Current public release	Receptor assets only; not equipment-failure data.
Fire perimeters	CAL FIRE FRAP	Perimeter polygons with cause fields	2017–2023 subset	Exposure labels; not damage or outage observations.
gridMET	University of Idaho gridMET	Daily weather, annual summaries	2017–2023	Observed annual weather covariates.
LANDFIRE	LANDFIRE LF2024	Fuel and canopy rasters	LF2024	Static fuel-structure covariates; time-matched sensitivity is needed.
USGS 3DEP	USGS 3DEP	Elevation raster	Current public DEM	Terrain covariate; not a fire-spread model.

Four annual labels are retained (Table 2). The all-fire label records any perimeter overlap. The exogenous label is the main target. The strict label further excludes Equipment Use. Electrical-power overlap is a diagnostic only and is not interpreted as ignition probability.

Table 2: Annual segment-year labels. Labels are not mutually exclusive because multiple perimeters can overlap a segment-year.

Label	Definition	Positives	Interpretation
All-fire exposure	Any 1 km segment-buffer intersection with a CAL FIRE perimeter	3,187	Broad exposure screen.
Exogenous exposure	Any overlap after excluding CAUSE = 11	2,331	Main external exposure target.
Strict exogenous exposure	Excludes CAUSE in {Electrical Power, Equipment Use}	2,075	Sensitivity label.
Electrical-power overlap	Any overlap with CAUSE = 11	885	Diagnostic only.
Mixed exogenous/electrical rows	Segment-years with both exogenous and electrical-power overlaps	29	Multiple-fire overlap diagnostic.

Figure 2: Cause-screened exposure labels used for receptor-asset validation.

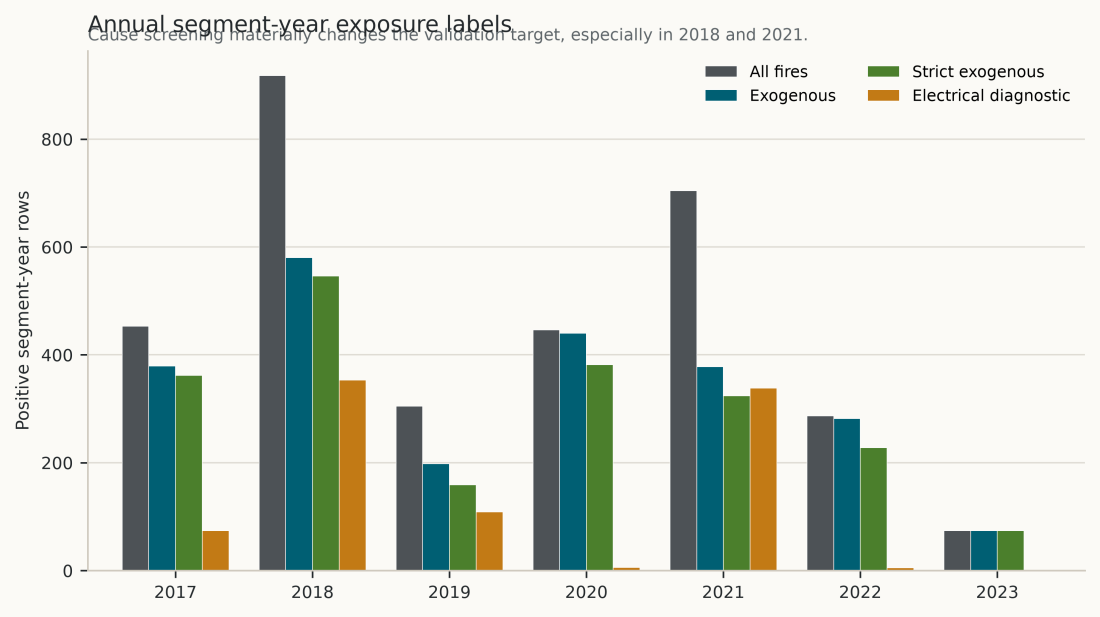

Figure 3: Annual segment-year label counts.

4 Methods

4.1 Covariate Construction

The feature core combines observed annual gridMET dryness and wind summaries, USGS terrain, LANDFIRE canopy/fuel-structure variables, and simple physics-guided indices. VPD and related fuel-aridity metrics have established links to western-US fire activity (Abatzoglou and Williams, 2016). ERC and BI are National Fire Danger Rating System quantities (Deeming et al., 1977); recent NFDRS modernization has also emphasized improved live- and dead-fuel-moisture calculations (Jolly et al., 2024). The engineered indices below are study-specific standardized composites, not official NFDRS indices.

Let $z(\cdot)$ denote training-period standardization. The dryness index is

$$d_{it} = \frac{z(\mathrm{VPD}_{it}) + z(\mathrm{ERC}_{it}) + z(\mathrm{BI}_{it}) + z(\mathrm{wind}_{it})}{4} - \frac{z(\mathrm{FM100}_{it}) + z(\mathrm{FM1000}_{it}) + z(\mathrm{RMIN}_{it}) + z(\mathrm{PR}_{it})}{4}. \tag{2}$$

The fuel-structure index is

$$f_i = \frac{z(\text{canopy cover}_i) + z(\text{canopy height}_i) + z(\text{canopy bulk density}_i)}{3}. \tag{3}$$

The selected core contains the raw public covariates, d_{it}, f_i, and $d_{it}f_i$. Canopy base height is included as an additional selected model covariate but is not part of the fuel-structure index in this specification. Because d_{it} and f_i are linear composites of raw standardized covariates, individual coefficients are not interpreted; the physics-guided nonlinear information enters through the interaction $d_{it}f_i$. LANDFIRE FBFM40 is categorical and is not used in the selected Bayesian or L2 logistic core.

Table 3: Exact construction of model covariates. Spatial extraction follows the processing scripts: gridMET annual aggregates are sampled from the nearest grid cell to the segment midpoint; raster covariates are sampled at the segment midpoint.

Variable	Source	Raw unit	Temporal aggregation	Spatial extraction	Role/sign in engineered index
VPD	gridMET	kPa	annual p95	nearest cell to segment midpoint	dryness, positive
ERC	gridMET	NFDRS index	annual p95	nearest cell to segment midpoint	dryness, positive
BI	gridMET	NFDRS index	annual p95	nearest cell to segment midpoint	dryness, positive
wind	gridMET	m s^{-1}	annual p95	nearest cell to segment midpoint	dryness, positive
FM100	gridMET	percent	annual p05	nearest cell to segment midpoint	dryness, negative
FM1000	gridMET	percent	annual p05	nearest cell to segment midpoint	dryness, negative
RMIN	gridMET	percent	annual p05	nearest cell to segment midpoint	dryness, negative
PR	gridMET	mm	annual sum	nearest cell to segment midpoint	dryness, negative
elevation	USGS 3DEP	m	static	raster sample at segment midpoint	deterministic score, positive
canopy cover	LANDFIRE LF2024	percent	static	raster sample at segment midpoint	fuel index, positive
canopy height	LANDFIRE LF2024	raw/10 m	static	raster sample at segment midpoint	fuel index, positive
canopy base height	LANDFIRE LF2024	raw/10 m	static	raster sample at segment midpoint	selected model covariate; not in fuel index
canopy bulk density	LANDFIRE LF2024	raw/100 kg m^{-3}	static	raster sample at segment midpoint	fuel index, positive

4.2 Deterministic Comparator

The deterministic comparator is a transparent, calibrated physics-guided score:

$$r_{it}^{det} = 0.56 d_{it} + 0.30 f_i + 0.14 z(\text{elevation}_i). \tag{4}$$

The weights were fixed as an a priori transparent heuristic comparator and were not optimized on the 2022–2023 holdout. The raw score is clipped to the training-period 1st–99th percentile range and scaled to $[0, 1]$:

$$s_{it}^{det} = \frac{\text{clip}\left(r_{it}^{det}, q_{0.01}^{train}, q_{0.99}^{train}\right) - q_{0.01}^{train}}{q_{0.99}^{train} - q_{0.01}^{train}}. \tag{5}$$

It is then calibrated with a regularized logistic model,

$$p_{it}^{det} = \text{logit}^{-1}(\gamma_0 + \gamma_1 s_{it}^{det}). \tag{6}$$

This gives a single score and calibrated point probability but no posterior distribution over ranks.

4.3 Bayesian and L2 Logistic Models

The Bayesian exposure model is a weakly regularized logistic regression:

$$y_{it}^{exo} \sim \text{Bernoulli}(p_{it}), \tag{7}$$

$$p_{it} = \text{logit}^{-1}(\alpha + \mathbf{x}_{it}^{\top}\boldsymbol{\beta}), \tag{8}$$

$$\alpha \sim \mathcal{N}(0, 5^2), \qquad \beta_k \sim \mathcal{N}(0, 2^2). \tag{9}$$

The exact design vector is

$$\begin{aligned} \mathbf{x}_{it} = [&z(\text{VPD}), z(\text{ERC}), z(\text{BI}), z(\text{wind}), \\ &z(\text{FM100}), z(\text{FM1000}), z(\text{RMIN}), z(\text{PR}), \\ &z(\text{elevation}), z(\text{canopy cover}), z(\text{canopy height}), \\ &z(\text{canopy base height}), z(\text{canopy bulk density}), d_{it}, f_i, d_{it} f_i]^{\top}. \end{aligned} \tag{10}$$

All entries are centered and scaled using the 2017–2021 training rows before model fitting. Weakly informative regularization is commonly used to stabilize logistic regression coefficients (Gelman et al., 2008). The posterior is approximated by a Laplace approximation around the posterior mode $\hat{\theta}$,

$$p(\theta \mid \mathcal{D}) \approx \mathcal{N}\left(\hat{\theta},\ H(\hat{\theta})^{-1}\right), \tag{11}$$

where $H(\hat{\theta})$ is the negative Hessian of the log posterior (Tierney and Kadane, 1986). A Gaussian prior on coefficients is equivalent to an L2 penalty at the posterior mode; similar discrimination between Bayesian Laplace and L2 logistic is therefore expected. The Bayesian layer is retained because posterior draws support rank and threshold decision quantities.

For posterior draw s, segment exposure over holdout years $T^{\star}$ is

$$\bar{p}_i^{(s)} = \frac{1}{|T^{\star}|} \sum_{t \in T^{\star}} \text{logit}^{-1}\left(\alpha^{(s)} + \mathbf{x}_{it}^{\top}\boldsymbol{\beta}^{(s)}\right). \tag{12}$$

The decision quantities are

$$q_i = P(\bar{p}_i > \tau \mid \mathcal{D}) \approx \frac{1}{S}\sum_{s=1}^{S} \mathbf{1}\{\bar{p}_i^{(s)} > \tau\}, \tag{13}$$

$$\rho_i = P(\mathrm{rank}_{\downarrow}(\bar{p}_i) \le K \mid \mathcal{D}) \approx \frac{1}{S}\sum_{s=1}^{S} \mathbf{1}\{\mathrm{rank}_{\downarrow}(\bar{p}_i^{(s)}) \le K\}. \tag{14}$$

Here $\tau = \pi_{train}$ is the training-period prevalence, $K = \lceil 0.1N \rceil$, and $\mathrm{rank}_{\downarrow}$ denotes descending exposure rank.

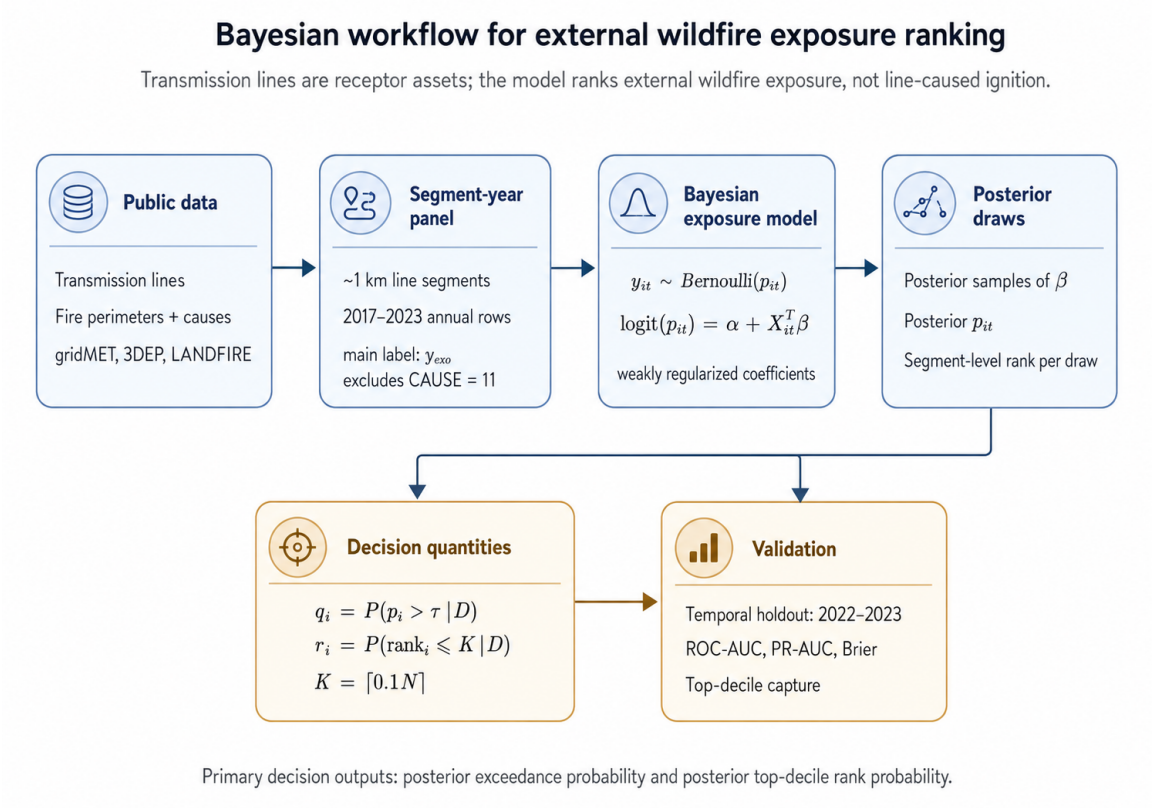

Figure 4: Bayesian workflow for posterior exposure probability and posterior top-decile rank probability.

4.4 Baseline Models and Implementation

All non-Bayesian baselines are fitted with fixed scikit-learn specifications using the same selected physics core. No hyperparameter is selected using the 2022–2023 comparison. Table 4 records the implementation details needed to reproduce the reported baselines.

4.5 Validation Design

Models are trained on 2017–2021 and evaluated on 2022–2023. The holdout set contains 22,510 segment-year rows and 356 exogenous exposure positives, giving a holdout prevalence of 1.5815%.

Table 4: Baseline model implementations.

Model	Implementation	Class handling	Key fixed parameters
Logistic L2	StandardScaler + sklearn LogisticRegression	Default class weights	solver = lbfgs; C = 1; max_iter = 2000; seed = 20260701
Balanced random forest	sklearn RandomForestClassifier	class_weight = balanced_subsample	n_estimators = 450; min_samples_leaf = 12; n_jobs = -1; seed = 20260701
Balanced extra trees	sklearn ExtraTreesClassifier	class_weight = balanced	n_estimators = 450; min_samples_leaf = 12; n_jobs = -1; seed = 20260701
Histogram gradient boosting	sklearn HistGradientBoostingClassifier	No explicit class weighting	max_iter = 260; learning_rate = 0.035; max_leaf_nodes = 24; l2_regularization = 0.05; seed = 20260701

Precision-recall performance is emphasized alongside ROC-AUC because PR curves are more informative under heavy class imbalance (Saito and Rehmsmeier, 2015). Probabilistic accuracy is summarized with the Brier score (Brier, 1950). Brier skill is reported against the out-of-sample constant probability defined by the training prevalence, while the holdout-prevalence constant is reported only as a hindsight reference.

As a preliminary uncertainty check on metric differences, we also compute $B = 120$ paired segment-cluster bootstrap replicates. Each replicate resamples segment IDs with replacement, retains all holdout-year rows for selected segments, and recomputes paired PR-AUC and Capture@10 differences. Intervals are 2.5th–97.5th bootstrap percentiles. This check is not a replacement for spatial block validation.

5 Results

5.1 Temporal Holdout Performance

Table 5 summarizes temporal-holdout performance. Bayesian Laplace and L2 logistic have similar discrimination. In this split, their top-ranked tails capture more holdout positives than the deterministic comparator, while the Bayesian point prediction is not materially better than L2 logistic. The Bayesian contribution is therefore interpreted as a posterior decision layer rather than as broad classification superiority. An initial Stan run reproduced the Laplace point-ranking metrics; full convergence summaries and posterior predictive diagnostics remain future work.

Table 5: Temporal-holdout comparison for 2022–2023 exogenous exposure.

Model	ROC-AUC	PR-AUC	Brier	Row top 10%	Segment top 10%
ML logistic L2	0.663	0.039	0.015713	0.289	0.216
Bayesian Laplace	0.662	0.038	0.015718	0.289	0.216
Deterministic calibrated	0.651	0.028	0.015734	0.219	0.118
Balanced extra trees	0.617	0.022	0.056091	0.180	0.104
Histogram gradient boosting	0.553	0.019	0.016647	0.132	0.149
Balanced random forest	0.568	0.018	0.034539	0.107	0.152

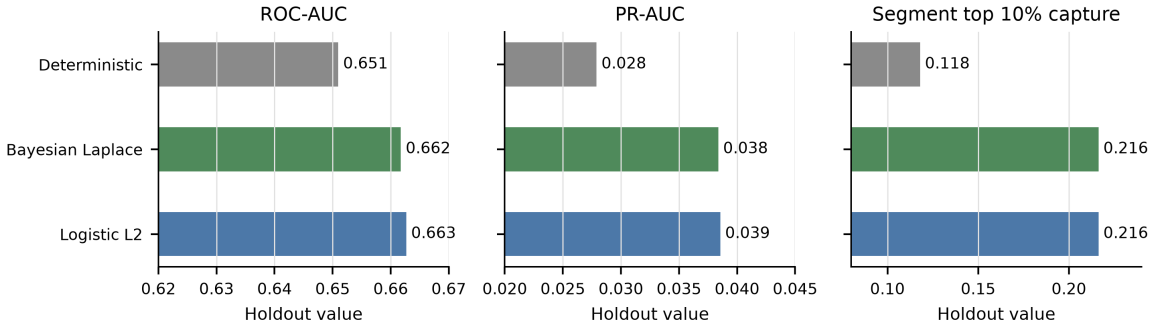

Figure 5: Key 2022–2023 temporal-holdout metrics for the deterministic comparator, Bayesian Laplace posterior mean, and L2 logistic baseline.

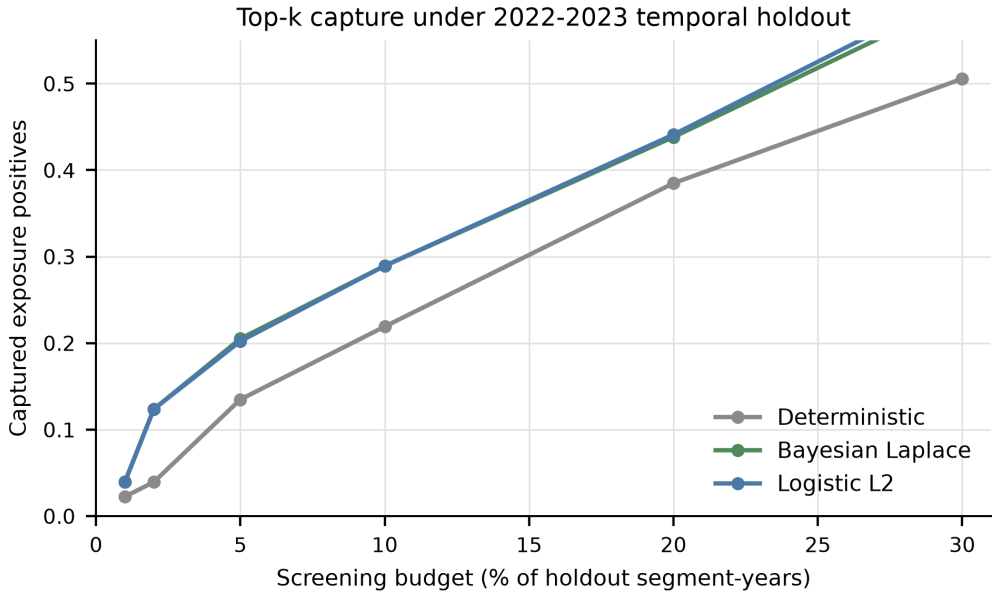

Figure 6: Top-k capture curve under the 2022–2023 temporal holdout. Bayesian Laplace and L2 logistic rankings are close; both select more observed exposure positives than the deterministic comparator in the top-ranked tail of this split.

Table 6: Rare-event probability baseline audit. Training prevalence is 1,975 / 56,275 = 3.5096%, giving a training-prevalence constant Brier score of 0.015937 on the holdout. The holdout-prevalence constant reference is 0.015565 and is available only in hindsight.

Model	PR-AUC	PR-AUC / π_{test}	Brier	BSS vs π_{train}
Logistic L2	0.03855	2.438	0.015713	0.0140
Bayesian Laplace	0.03838	2.427	0.015718	0.0138
Deterministic calibrated	0.02790	1.764	0.015734	0.0127

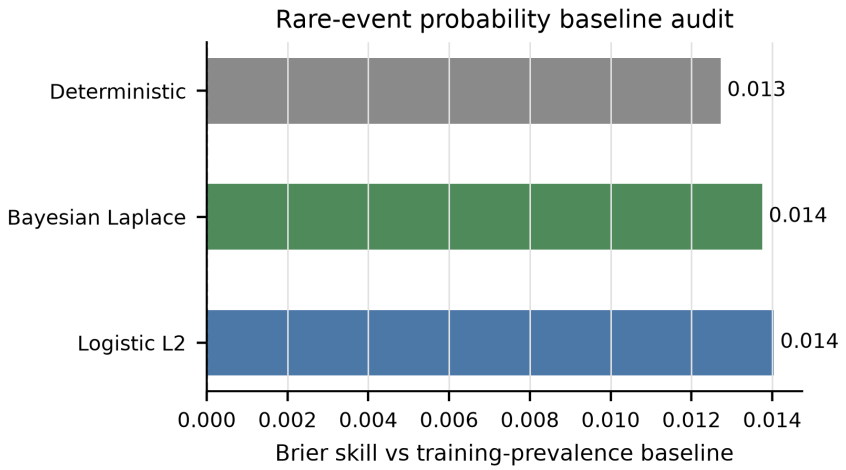

Figure 7: Brier skill relative to the training-prevalence constant probability baseline.

5.2 Posterior Decision Maps and Method Diagnostics

The posterior map output should be read as an uncertainty-aware exposure-ranking diagnostic. In particular, $\rho_i = P(\text{rank}_{\downarrow} \leq K \mid \mathcal{D})$ identifies segments that repeatedly fall into the top decile under posterior draws. Figure 8 shows the posterior decision metrics.

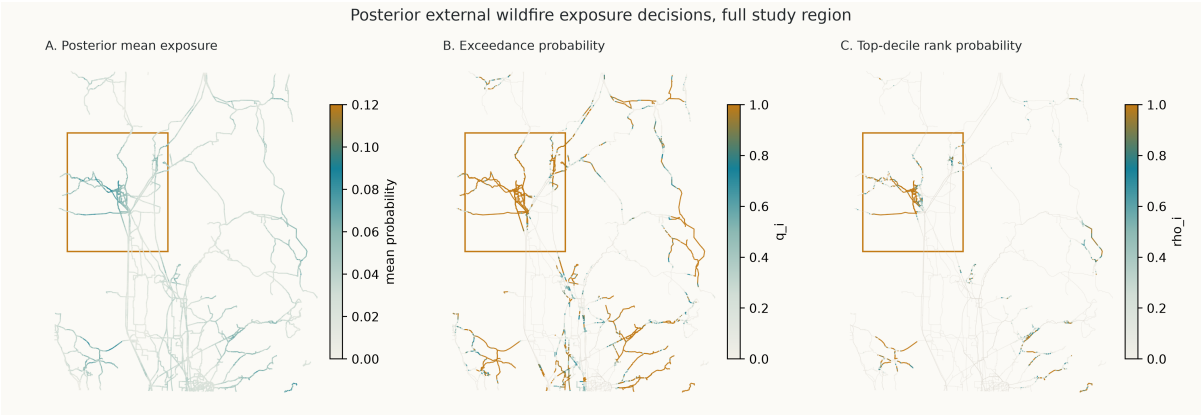

Figure 8: Full-region maps of posterior mean exposure probability, posterior exceedance probability, and posterior top-decile rank probability.

Table 7 summarizes the segment-level decision-set implication of ρ_i. The stable top-decile set contains 781 segments with $\rho_i \geq 0.9$, while 708 segments fall into the rank-uncertain interval $0.1 < \rho_i < 0.9$. The point-estimate top decile contains 1,126 segments, but its Jaccard overlap with the stable posterior top-decile set is 0.694; 27 point-top-decile segments have $\rho_i < 0.5$. This shows that a single ranked list hides decision-relevant rank uncertainty even when point discrimination is similar to L2 logistic.

The selected Bayesian and L2 logistic core does not use FBFM40. The processed CH, CBH, and CBD columns are positive constant scalings of decoded physical units; because the selected linear core standardizes these variables before fitting, decoding does not require rerunning the selected Bayesian/L2 model. This no-rerun statement does not apply to threshold rules or tree

Table 7: Posterior rank uncertainty groups evaluated against 2022–2023 observed segment exposure.

Posterior rank group	Segments	Observed exposed segments	Exposure frequency
Stable top-decile ($\rho_i \geq 0.9$)	781	41	0.0525
Rank-uncertain ($0.1 < \rho_i < 0.9$)	708	46	0.0650
Stable lower rank ($\rho_i \leq 0.1$)	9,766	264	0.0270

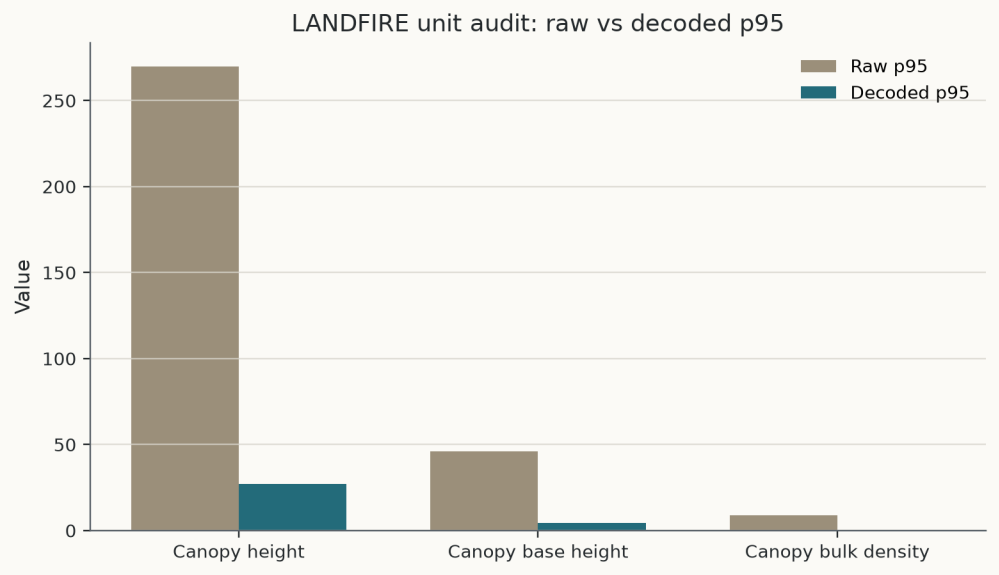

Figure 9: LANDFIRE unit audit for canopy height, canopy base height, and canopy bulk density.

models. Because feature-core selection was not evaluated with a nested temporal selection design, the 2022–2023 comparison should be interpreted as a retrospective model comparison rather than a locked final-test estimate.

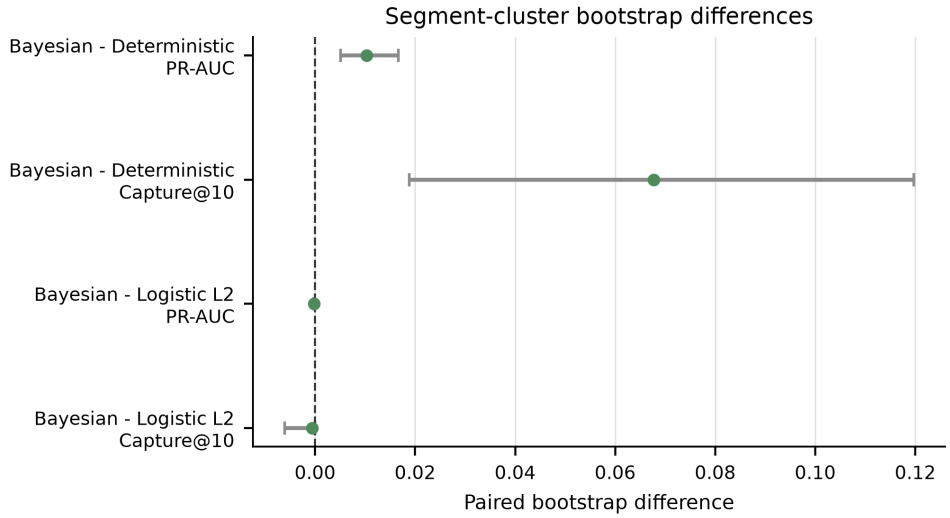

Figure 10: Paired segment-cluster bootstrap differences for PR-AUC and Capture@10. Bayesian Laplace improves Capture@10 relative to the deterministic comparator in this split, while Bayesian Laplace and L2 logistic are nearly indistinguishable by this check.

6 Discussion

The main result is bounded. Public data can support a reproducible, screening-level framework for retrospective external wildfire exposure ranking of transmission-line receptor assets. The output is a ranked exposure screen, not a statement about ignition causality, equipment condition, outage, damage, or responsibility.

The temporal-holdout results do not show broad Bayesian classification superiority. L2 logistic and Bayesian Laplace have nearly identical ROC-AUC, PR-AUC, Brier score, and top-decile capture. This is consistent with the relationship between Gaussian-prior logistic regression and L2 penalization. The Bayesian contribution is instead decision-facing: posterior draws convert a fitted exposure model into posterior exceedance probability and posterior top-decile rank probability.

The deterministic comparator remains useful because it is transparent and easy to audit. Its limitation is that it gives one ranking without posterior rank uncertainty. Flexible tree-based ML baselines do not improve this temporal holdout, but this result should be interpreted cautiously. It supports careful feature design and temporal validation, not a general rejection of ML.

Existing wildfire risk tools target different questions. Powerline ignition models generally require private utility data and address grid-to-fire causality (Yao et al., 2022). Fire-to-grid and grid-impact studies address consequences for electricity systems (Dale et al., 2018; Panossian and Elgindy, 2023). Physical and quasi-physical fire-spread models target propagation dynamics and require a different set of process and scenario assumptions (Sullivan, 2009). The present framework occupies a narrower space: public-data fire-to-grid external exposure ranking with a posterior decision layer.

7 Limitations

Several limitations are important. First, the pipeline estimates external exposure only. It does not estimate ignition causality, equipment failure, outage probability, damage, or legal responsibility. Second, the CAL FIRE cause field is a perimeter-level attribute; electrical-power overlap is therefore only a diagnostic label. Third, LF2024 static fuel layers may be temporally mismatched with 2017–2023 exposure years (LANDFIRE, 2025). Fourth, FBFM40 must be encoded categorically or removed from final ablations. Fifth, the label uses a fixed 1 km buffer, so buffer-radius sensitivity remains a model-definition sensitivity. Sixth, temporal holdout does not remove spatial dependence among neighboring segments. Blocked validation is recommended when spatial or hierarchical dependence structures are present (Roberts et al., 2017); spatially separated folds can be operationalized with block-based procedures (Valavi et al., 2019). Finally, the Stan run is a pilot; full diagnostics, longer chains, convergence summaries, and posterior predictive checks remain necessary for stronger Bayesian computation claims.

8 Conclusion

This paper presents a public-data framework for retrospective external wildfire exposure ranking of transmission-line receptor assets. The workflow builds a 2017–2023 segment-year panel, uses cause-screened exposure labels, and compares deterministic, Bayesian, and machine-learning baselines under a 2022–2023 temporal holdout. Bayesian and L2 logistic point-prediction performance is similar. The Bayesian formulation adds posterior exceedance and posterior top-decile rank probabilities, with posterior rank probability emphasized as the main decision quantity. The framework should not be interpreted as a powerline ignition, equipment-failure, outage, damage, or responsibility model.

A Posterior Map Zoom

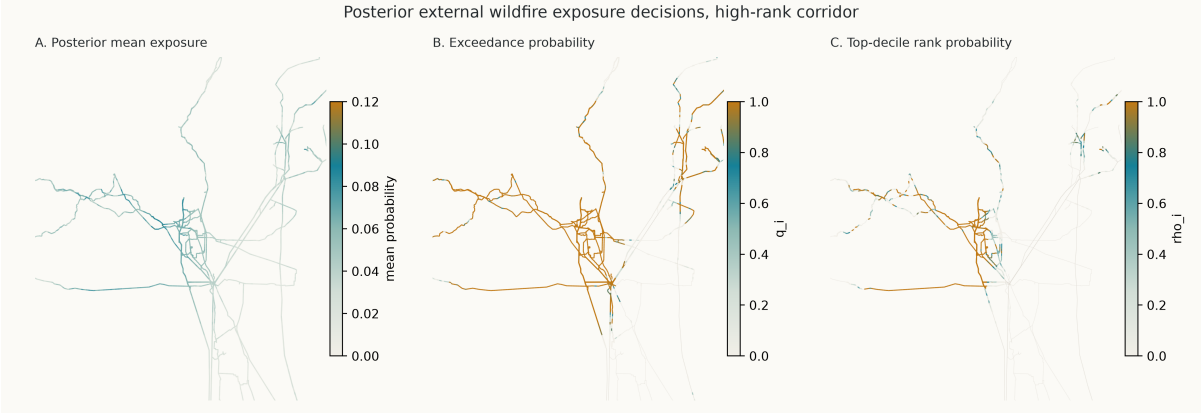

Figure 11: Zoomed high-rank corridor for posterior mean exposure probability, posterior exceedance probability, and posterior top-decile rank probability.

B Covariate Diagnostics

The following maps document the public covariate layers used to construct dynamic weather, terrain, and fuel-structure predictors. They are included as covariate-diagnostic figures rather than as separate scientific claims.

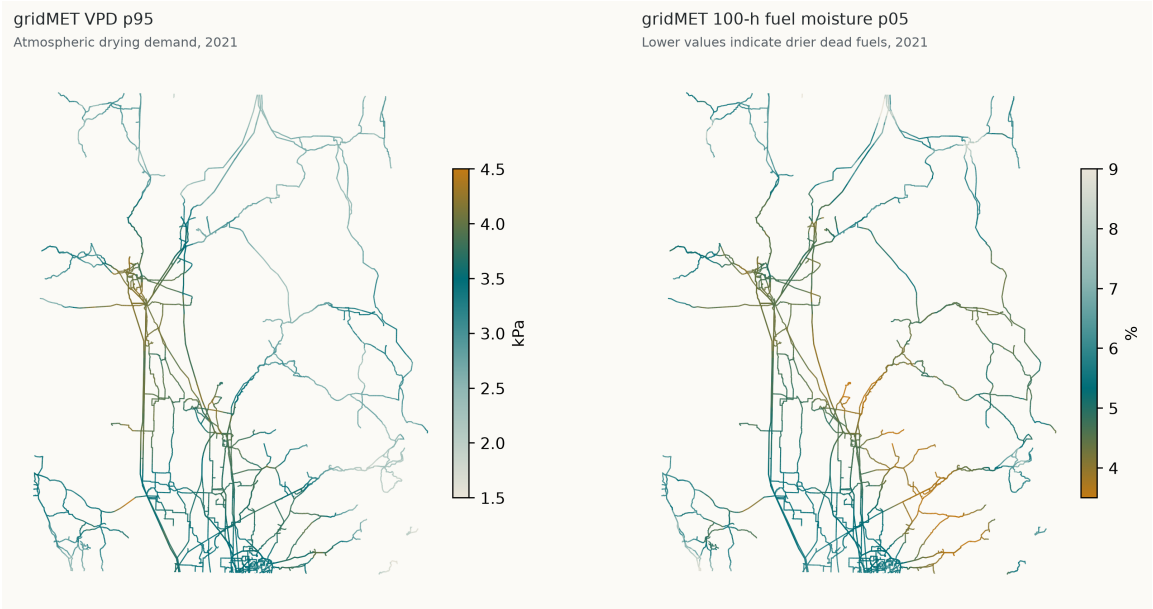

Figure 12: gridMET annual fire-weather covariate layers for 2021.

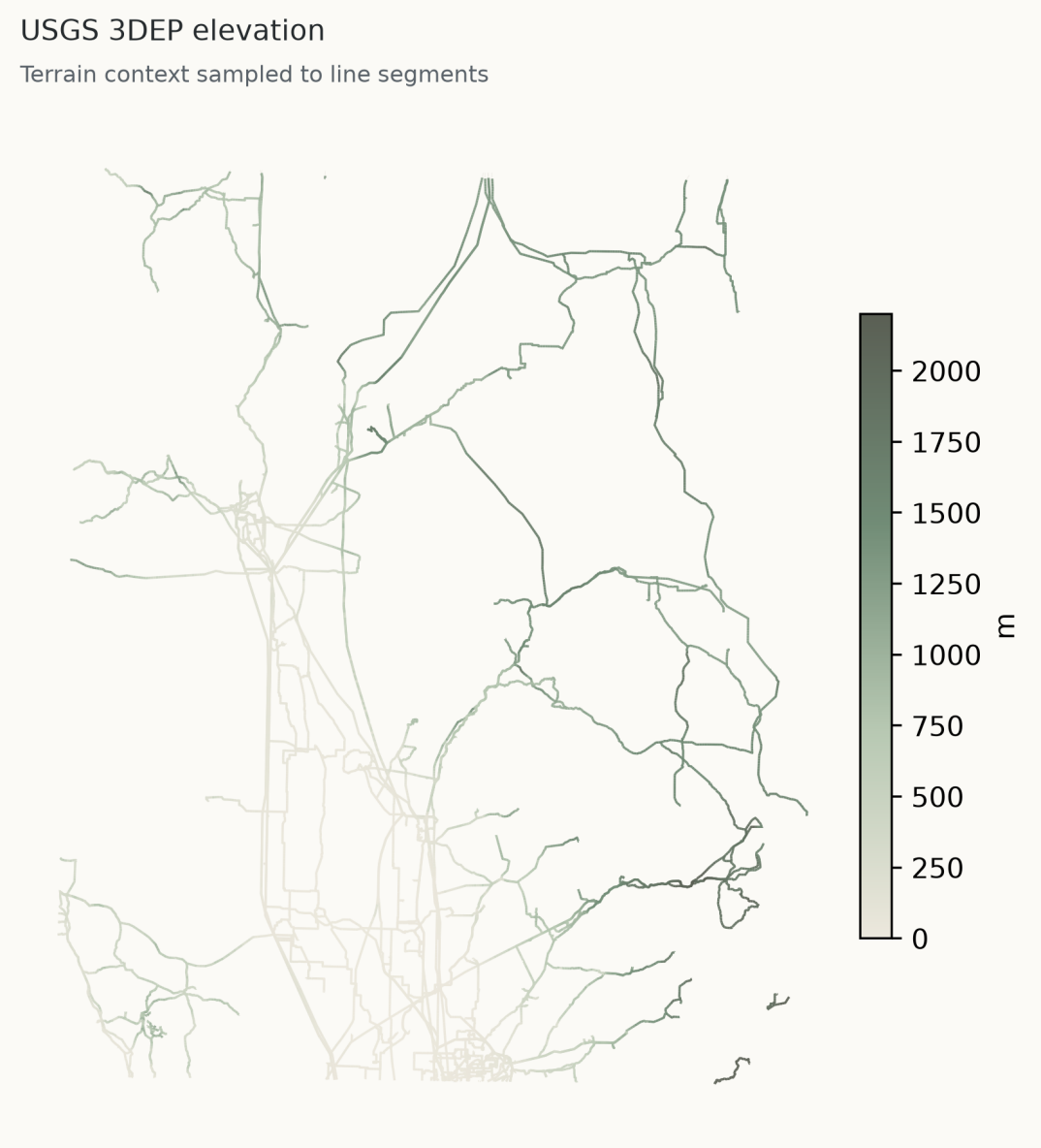

Figure 13: USGS 3DEP terrain covariate layer.

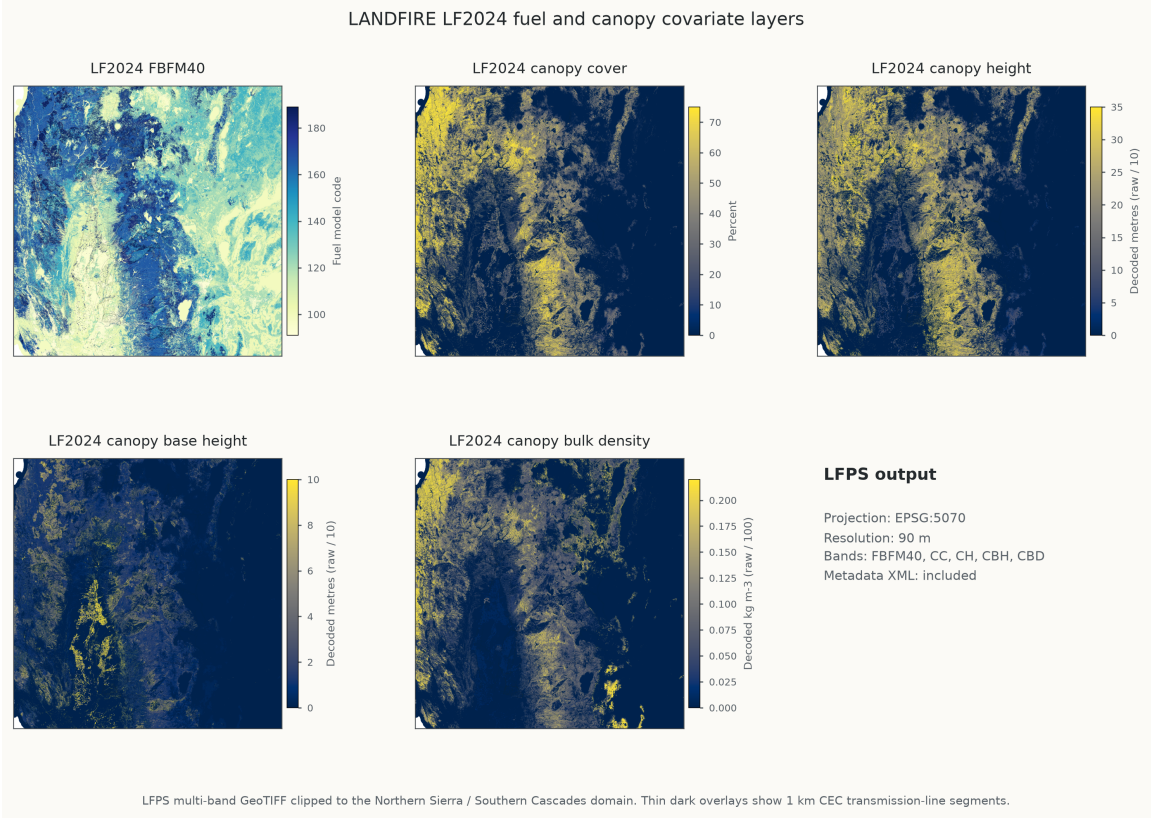

Figure 14: LANDFIRE LF2024 fuel and canopy covariate layers with decoded CH, CBH, and CBD units.

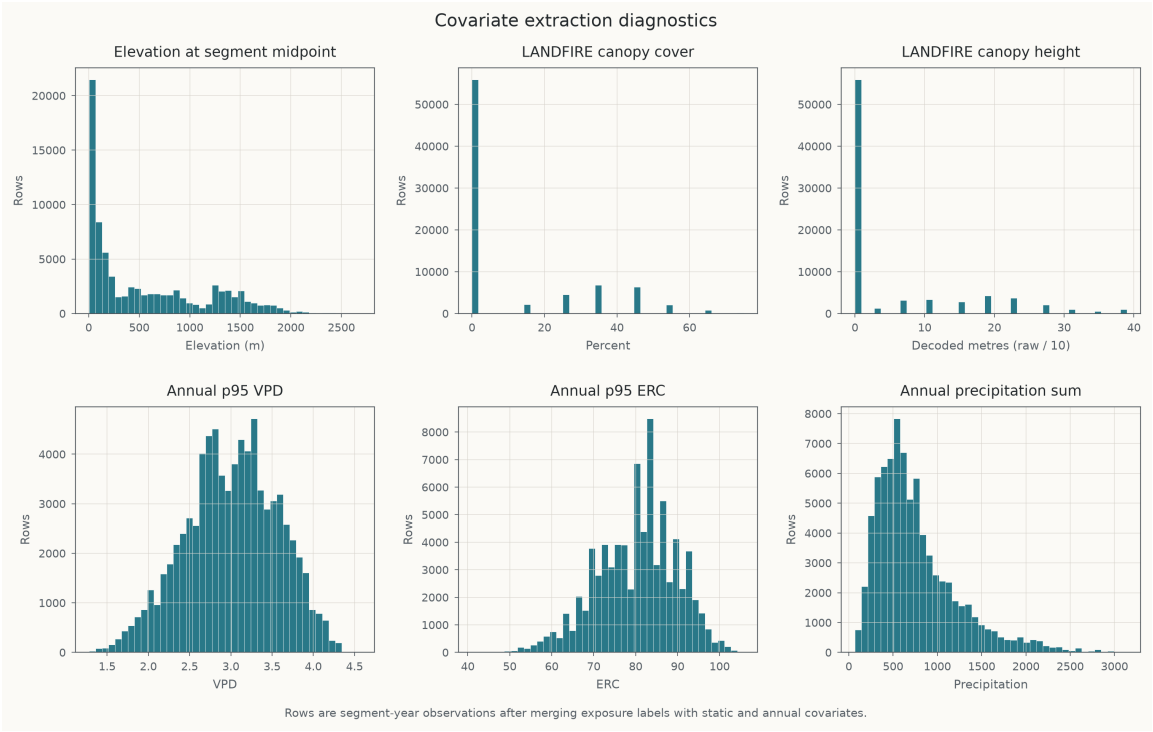

Figure 15: Covariate distribution diagnostics with decoded LANDFIRE canopy height units.

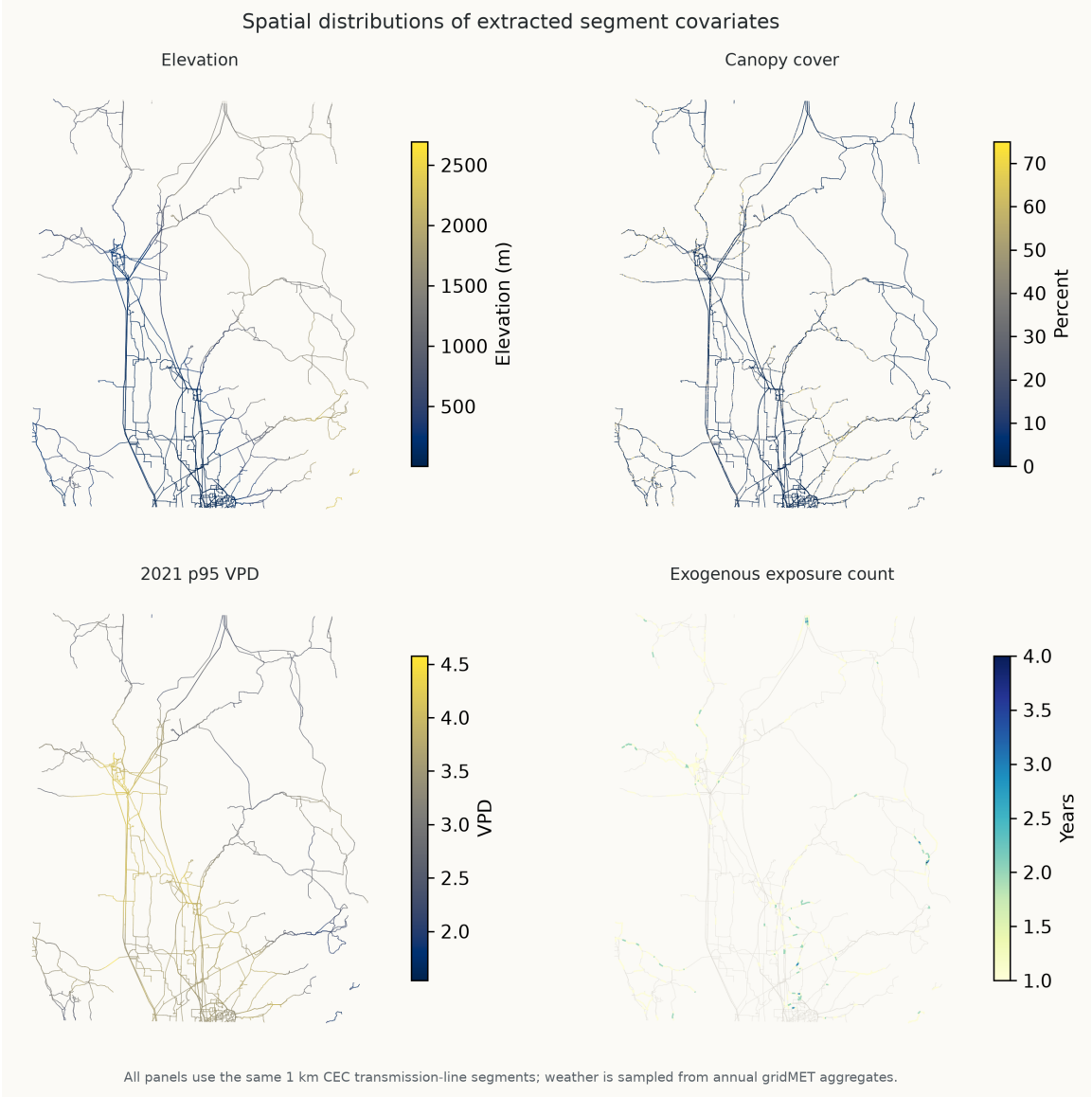

Figure 16: Spatial covariate distributions.

References

John T. Abatzoglou. Development of gridded surface meteorological data for ecological applications and modelling. *International Journal of Climatology*, 33(1):121–131, 2013. doi: 10.1002/joc.3413.

John T. Abatzoglou and A. Park Williams. Impact of anthropogenic climate change on wildfire across western US forests. *Proceedings of the National Academy of Sciences of the United States of America*, 113(42):11770–11775, 2016. doi: 10.1073/pnas.1607171113.

Glenn W. Brier. Verification of forecasts expressed in terms of probability. *Monthly Weather Review*, 78(1):1–3, 1950. doi: 10.1175/1520-0493(1950)078<0001:VOFEIT>2.0.CO;2.

California Department of Forestry and Fire Protection, Fire and Resource Assessment Program. Fire perimeters. CAL FIRE FRAP, 2026. URL https://www.fire.ca.gov/what-we-do/fire-resource-assessment-program/fire-perimeters. Historical fire perimeter dataset; fire25.1 geodatabase used in the present workflow; accessed 2026-07-07.

California Energy Commission. California electric transmission lines. California Energy Commission GIS Open Data, 2026. URL https://cecgis-caenergy.opendata.arcgis.com/datasets/CAEnergy::california-electric-transmission-lines-1. Current public release; accessed 2026-07-07.

Larry Dale, Michael Carnall, Gary Fitts, Sarah Lewis McDonald, and Max Wei. Assessing the impact of wildfires on the california electricity grid. Technical Report CCCA4-CEC-2018-002, California Energy Commission, 2018. California's Fourth Climate Change Assessment.

John E. Deeming, Robert E. Burgan, and Jack D. Cohen. The national fire-danger rating system – 1978. Technical Report General Technical Report INT-39, U.S. Department of Agriculture, Forest Service, Intermountain Forest and Range Experiment Station, Ogden, Utah, 1977.

Andrew Gelman, Aleks Jakulin, Maria Grazia Pittau, and Yu-Sung Su. A weakly informative default prior distribution for logistic and other regression models. *The Annals of Applied Statistics*, 2(4):1360–1383, 2008. doi: 10.1214/08-AOAS191.

W. Matt Jolly, Patrick H. Freeborn, Larry S. Bradshaw, Jon Wallace, and Stuart Brittain. Modernizing the US national fire danger rating system (version 4): Simplified fuel models and improved live and dead fuel moisture calculations. *Environmental Modelling & Software*, 181:106181, 2024. doi: 10.1016/j.envsoft.2024.106181.

LANDFIRE. LANDFIRE 2024 Update. LANDFIRE program documentation, 2025. URL https://landfire.gov/data/lf2024. LF2024 product-suite documentation; accessed 2026-07-07.

LANDFIRE. LANDFIRE Dictionary, Version 1.0. LANDFIRE program documentation, 2026. URL https://landfire.gov/data-downloads/documents/LF_Data_Dictionary.pdf. Guide to LANDFIRE products, attribute data dictionaries, data standards, and terminology; accessed 2026-07-07.

Nadia Panossian and Tarek Elgindy. Power system wildfire risks and potential solutions: A literature review & proposed metric. Technical Report NREL/TP-6A40-80746, National Renewable Energy Laboratory, Golden, Colorado, 2023.

David R. Roberts, Volker Bahn, Simone Ciuti, Mark S. Boyce, Jane Elith, Gurutzeta Guillera-Arroita, Severin Hauenstein, José J. Lahoz-Monfort, Boris Schröder, Wilfried Thuiller, David I. Warton, Brendan A. Wintle, Florian Hartig, and Carsten F. Dormann. Cross-validation strategies for data with temporal, spatial, hierarchical, or phylogenetic structure. *Ecography*, 40(8):913–929, 2017. doi: 10.1111/ecog.02881.

Matthew G. Rollins. LANDFIRE: A nationally consistent vegetation, wildland fire, and fuel assessment. *International Journal of Wildland Fire*, 18(3):235–249, 2009. doi: 10.1071/WF08088.

Takaya Saito and Marc Rehmsmeier. The precision-recall plot is more informative than the ROC plot when evaluating binary classifiers on imbalanced datasets. *PLOS ONE*, 10(3):e0118432, 2015. doi: 10.1371/journal.pone.0118432.

Andrew L. Sullivan. Wildland surface fire spread modelling, 1990–2007. 1: Physical and quasi-physical models. *International Journal of Wildland Fire*, 18(4):349–368, 2009. doi: 10.1071/WF06143.

Luke Tierney and Joseph B. Kadane. Accurate approximations for posterior moments and marginal densities. *Journal of the American Statistical Association*, 81(393):82–86, 1986. doi: 10.1080/01621459.1986.10478240.

U.S. Geological Survey. 1/3rd arc-second digital elevation models (DEMs) – USGS national map 3d elevation program downloadable data collection. U.S. Geological Survey Data Catalog, 2026. URL https://data.usgs.gov/datacatalog/data/USGS:3a81321b-c153-416f-98b7-cc8e5f0e17c3. Approximately 10 m resolution 3DEP DEM collection; accessed 2026-07-07.

Roozbeh Valavi, Jane Elith, José J. Lahoz-Monfort, and Gurutzeta Guillera-Arroita. blockCV: An R package for generating spatially or environmentally separated folds for k-fold cross-validation of species distribution models. *Methods in Ecology and Evolution*, 10(2):225–232, 2019. doi: 10.1111/2041-210X.13107.

Mengqi Yao, Meghana Bharadwaj, Zheng Zhang, Baihong Jin, and Duncan S. Callaway. Predicting electricity infrastructure induced wildfire risk in california. *Environmental Research Letters*, 17(9):094035, 2022. doi: 10.1088/1748-9326/ac8d18.